

Formation of CsPbI₃ γ -Phase at 80 °C by Europium-Assisted Snowplow Effect

Alessandra Alberti,* Emanuele Smecca, Ioannis Deretzis, Giovanni Mannino, Corrado Bongiorno, Salvatore Valastro, Salvatore Sanzaro, Giuseppe Fisicaro, Ajay Kumar Jena, Youhei Numata, Zhanglin Guo, Corrado Spinella, Tsutomu Miyasaka, and Antonino La Magna

Herein, the convenient interplay between Eu incorporation and morphology to form the perovskite (PSK) γ -phase of CsPbI₃ at 80 °C (low temperature [LT] γ -phase) is unveiled. In contrast, CsPbI₃ without Eu exists in a mixture of γ -phase and non-PSK δ -phase at 65 °C or in a fully δ -phase at 80 °C. Based on experimental and theoretical findings, argued about a double beneficial role of Eu. On one hand, it assists in the formation of the γ -phase either by substituting Pb or by occupying interstitial positions in the CsPbI₃ lattice. On the other hand, it indirectly promotes the formation of a fine-grained layer at LT wherein the high surface-to-volume ratio makes the establishment of the δ -phase unfavorable. Strain accommodation in the fine-grained matrix and the formation of a gluing intergrain-self-material during the kinetics of reaction (snowplow effect) cooperate in extending the lifetime of the LT γ -phase to \approx 40 h at 65 °C compared to only \approx 10–15 min in the sample without Eu for the complete phase transformation. The disclosed phenomena draw a method for the stabilization of PSK-CsPbI₃ layers based on a self-generated thin frame of exceeding material filling the gaps between small-sized grains that can be used hereinafter to further extend the PSK lifetime.

constantly promoted the efficiency of PSCs. Easy compositional modifications accomplished by simple solution processing represent a huge strength to satisfy specific demands.^[1,2] Among many PSKs, MAPbI₃ (MA = methylammonium) is the first and most studied PSK material, and it is still under the spotlight, even though its stability has been found to be relatively lower with respect to many other compositions engineered later. Not only the stability of the material^[3–6] but also the durability of the interfaces with the TLs (electron-TL and hole-TL) are the main concerns for long-term stability of the cells.^[7–13] Partial replacement of MA with FA (FA = formamidinium) in mixed lattices improves the PSK durability^[14] and reliability. Anions are also mixed on purpose to exploit specific benefits such as, mixing bromides and iodides shifts the energy gap upward^[15] and increases the PSK structural stability. Material engineering

1. Introduction


Progress in the performance of perovskite solar cells (PSCs) is steadily advancing through device and compositional engineering. Different device architectures, various kinds of transporting layers (TLs), and the versatile perovskite (PSK) composition have

with multiple cations–anions and even “hollow”^[16] PSKs intend to boost PSCs’ efficiencies toward new records and, more importantly, to solve issues that are delaying the appearance of such technology in the market. It is in fact known that volatile organic cations in the hybrid PSKs are responsible for the thermal and environmental instabilities of the material.

Dr. A. Alberti, Dr. E. Smecca, Dr. I. Deretzis, Dr. G. Mannino, Dr. C. Bongiorno, Dr. S. Valastro, Dr. S. Sanzaro, Dr. G. Fisicaro, Dr. C. Spinella, Dr. A. La Magna
National Research Council-Institute for Microelectronics and Microsystems (CNR-IMM)
Zona Industriale Strada VIII n.5, Catania 95121, Italy
E-mail: alessandra.alberti@imm.cnr.it

Dr. S. Valastro
Dipartimento di Fisica e Astronomia
Università di Catania
Via S. Sofia 64, Catania 95123, Italy

Dr. A. K. Jena, Dr. Y. Numata, Dr. Z. Guo, Prof. T. Miyasaka
Graduate School of Engineering
Toin University of Yokohama
1614 Kurogane-cho, Aoba, Yokohama, Kanagawa 225-8503, Japan

 The ORCID identification number(s) for the author(s) of this article can be found under <https://doi.org/10.1002/aesr.202100091>.

© 2021 The Authors. Advanced Energy and Sustainability Research published by Wiley-VCH GmbH. This is an open access article under the terms of the Creative Commons Attribution License, which permits use, distribution and reproduction in any medium, provided the original work is properly cited.

DOI: 10.1002/aesr.202100091

In this scenario, Cs-based inorganic PSKs draw a special attention for their fully inorganic composition that, in principle, makes them more stable.^[17] With respect to use of organic cations, volatilization issues that cause local mass reduction and severe changes in morphology are minor concerns. In addition, Cs-based iodide PSKs energy gap around 1.7 eV fit the requirement for PSCs to work in tandem with silicon solar cells.^[18] In the pragmatic energetic landscape,^[19] it is often convenient to mix Cs with other organic cations to tune the bandgap and to gain a general benefit for the material reliability in devices. In recent years, all-inorganic PSK solar cells have made progress in terms of efficiency that has surpassed 19%.^[20] However, the phase stability of the material remains a challenge.

In addition to the non-PSK photoinactive δ -phase, CsPbI₃ exists in three PSK photoactive (called black) lattice structures:^[21] cubic α -phase, tetragonal β -phase and orthorhombic γ -phase stable at progressively descending temperatures, with the first one observed above 300 °C. However, several approaches have been followed to form the high temperature (HT) α -phase at lower temperatures, attempts have been also made to use the γ -phase that instead is stable at temperature relatively low (under \approx 180 °C). The γ -phase was even observed at room temperature but after quenching from HTs starting from the α -phase. Interestingly, it has been shown^[22] that CsPbI₃ is able to retain its γ -phase, once formed, from room temperature (RT) down to 100 K. The authors conclude, on the basis of X-ray diffraction (XRD) and pair distribution function analyses on single crystals, that rattling of the Cs cations, lower coordination of a second Cs site, and local octahedral distortion contribute to the thermodynamic instability of the CsPbI₃ γ -phase. Octahedral tilting is a configurational parameter that increases while the CsPbI₃ α -phase moves to the CsPbI₃ γ -phase. If this phase is left at RT, a full breaking of the PSK symmetry occurs and leads to the formation of the non-PSK δ -phase (yellow phase).^[23] Long-lasting accommodation of the octahedral tilting is a way to preserve the PSK phase. This strategy is adopted in PSK nanocrystals to stabilize the CsPbI₃ α -phase at RT using phosphonic acid or ammonium ligands or excess iodides or metal ions for doping.^[24–28]

The structural stability related to the lowest formation energy of the non-PSK δ -phase has hindered the maximum potential of CsPbI₃ PSCs.^[29] It represents an intrinsic limitation unless specific strategies are adopted to unbalance the equilibrium. This in principle could be done via volume and/or surface energy modifications, or alternatively by blocking the lattice in a PSK configuration. One approach, as anticipated, consists of raising the temperature of the δ -phase above 300 °C so as to activate the polymorphic transition to the cubic α -phase followed by a fast cooling to freeze a black PSK phase at RT as done by Straus et al.^[30] They used single crystals of CsPbI₃ blocked into the γ -phase after quenching from 370 °C in iced water. Nonetheless, long-lasting stability of out-of-equilibrium phases still rises some concerns, especially if the γ -phase grains have large size (low surface-to-volume ratio). The use of additives represents another way to follow, as done by Sutton et al.^[29] by introducing hydroiodic acid (HI) in the preparation procedure. This allowed forming the γ -phase at 100 °C with a fine-grained morphology compared with the γ -phase quenched from HT ($HT > 300$ °C). The authors also highlighted the importance of octahedral tilting and distortions on the stability of the PSK lattice.

In other strategies, the stabilization of PSK CsPbI₃ phases passes through chemical substitutions to change the energetic balance or to modify the cell volume via increasing the steric hindrance inside the unit cell^[29] or through a morphological control of the PSK grain size. Alternative strategies are reviewed in the study by Ye et al.^[31] where it is mentioned that stabilization of the CsPbI₃ phase is a consequence of a contraction of the PbX₆ octahedral volume (e.g., caused by Cs partial substitution with smaller cations) or based on interstitial doping with B-cations. Cover layers of various types and nature to stabilize the surface via passivation actions are also largely proposed in the literature.^[31]

All these findings suggest exploring strategies that favor octahedral accommodation via volume changes and/or doping and/or lattice defects to increase the tolerance of a PSK atomic arrangement. The choice of any strategy must, at the same time, satisfy the need of a low thermal budget that preserves other materials in the architecture and assure the integrability of PSCs into tandem solar cells. Hereinafter, we distinguish procedures that apply quenching from low temperature (LT) for γ -phase formation from the methods of quenching from HT, e.g., the one applied in the studies by Marronnier et al. and Straus et al.^[21,30]

In particular, LT formation and stabilization strategies should address a reduction of the volume-free energy for γ -phase formation on one side. On the other side, a gain in the surface-to-volume ratio balance to make unfavorable the establishment of the non-PSK δ -phase. Producing more distorted octahedra in stable γ -phase (e.g., I–Pb–I angle^[22]), acting on the distortion or controlling shape and dimension of the grains in the CsPbI₃ would be really viable routes.

With this aim and based on previous pioneering technological studies on the use of europium in the preparation procedure of CsPbI₃-based solar devices aimed at maximizing the photovoltaic performances,^[27] we undertake this investigation to unveil if and eventually how europium atoms have a role in the formation and stabilization of a PSK phase. The process control, lattice dynamics, Eu incorporation/topology as well as its role in the stabilization are totally unknown. We demonstrate the convenient interplay between Eu incorporation and morphology to stabilize the CsPbI₃ γ -phase at LT without passing through technologically unfeasible HT treatments. We set 80 °C for the γ -phase formation instead of HTs ($T > 300$ °C) found in the recent literature. In addition, we covered a large range of postformation temperature conditions, from -100 to 100 °C, to explore the γ -phase endurance. The study focused on clearly stating the phase formed in presence of Eu, its lattice arrangement and morphology, the competition among the phases, and finally, the structural stability of thin films (\approx 80 nm) with respect to single crystals, powders, and thick layers stabilized in the PSK phase by other methods. A general key-of-understanding is finally drawn that can be extended to other case studies or used for future strategies.

2. Results and Discussions

2.1. LT Phase Formation

The experiment is based on a comparative investigation of samples prepared with and without Eu. Samples “with Eu”

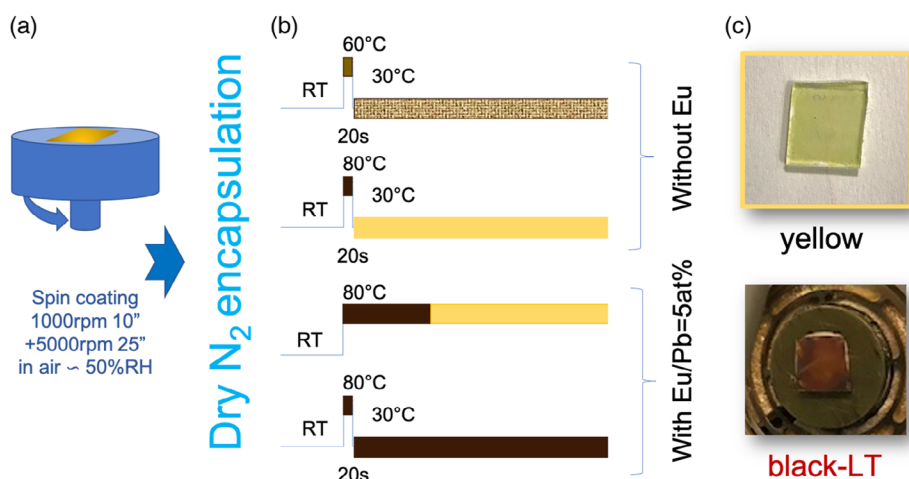


Figure 1. Schematic describing the approach to form a PSK CsPbI₃ phase at LT. a) Spin coating under air condition. b) Quenching procedures (0.5–1 °C s⁻¹) under dry N₂: without Eu precursor in the solution, 60 °C is the temperature to be used with the resulting material having a dark-yellow color; with Eu precursor in the spin-coated solution, the formation temperature is raised to 80 °C and the resulting material has a black color. In this second case, the sample is long lasting for days. c) Resulting materials: the black layer is 80–100 nm thick.

are prepared with Eu/Pb = 5% mixture based on the technological study reported in the paper by Jena et al.^[27] For sample preparation and reaction, we applied the protocol shown in **Figure 1**. It is based on spin coating in ambient conditions (RT ≈ 25 °C and relative humidity ≈ 50%) of a stoichiometric solution of PbI₂ and CsI that in addition eventually contains EuCl₃ with Eu/Pb = 5 at% (Figure 1a). The substrate is either glass or TiO₂/fluorine doped tin oxide (FTO). After spin coating, the sample is placed on a heating stage at a fixed temperature (60 or 80 °C) for 20 s (Figure 1b) and, immediately after, encapsulated under a dry-N₂ atmosphere. While keeping the temperature at 60–65 °C, the sample without Eu gains a dark-yellow color. Applying, instead, a higher temperature (e.g., 80 °C) produces pale-yellow colored samples typical of the δ-phase (Figure 1c topside). The samples were analyzed with several analytical techniques as hereafter discussed.

Conversely, a temperature of 80 °C applied to the sample prepared with Eu settles a fully black color. A lower temperature (e.g., 60–65 °C) leaves, instead, the sample yellow. In Figure 1, it is also represented that quenching the sample from 80 to 30 °C after 20s of annealing (0.5–1 °C s⁻¹) is mandatory to avoid further evolution of the black phase to yellow. Temperature and time effects will be explored in Section 2.5.

Even though the black color of the sample provides a qualitative feedback on the formation of a PSK phase (cubic-α or tetragonal-β or orthorhombic-γ), its precise identification needs quantitative measurements. This sample was indeed initially labeled as “black low temperature” (black-LT) PSK phase to be distinguished from black HT (black-HT) PSK formed at $T > 300$ °C.

The first clue about the stabilization of the black phase at LT that cannot be attributed to Cl atoms was provided by preliminary tests. In particular, when replacing small amounts of PbI₂ with PbCl₂ (5 mol%), or CsI with CsCl (5 mol%) and even adding HCl (10 μL into 500 μL CsPbI₃ solution), a yellow phase is formed in all three cases^[27] without CsPbCl₃ detected.^[32] In contrast, the substitution of EuCl₃ with EuI₂ has produced

the black phase of CsPbI₃ following the preparation procedure shown in Figure 1a,b, with similar morphology and structure. In the end, the beneficial main role of Eu was argued compared with Cl. Although both EuI₂ and EuCl₃ produced a black phase at LT, it has been observed that EuCl₃ has a better solubility. We have indeed chosen to carry out detailed cross-correlated investigation using EuCl₃, like Jena et al.^[27] had done for their pioneering technological study, with some focused comparative experiments using EuI₂.

2.2. LT γ-Phase Structure

The structure of the deposited materials was investigated by XRD on samples encapsulated in dry-N₂ immediately after quenching to 30 °C to avoid humidity-related effects; moreover, the analyses were repeated on different samples using glass or TiO₂/FTO as substrates.

Based on the XRD pattern shown in **Figure 2a** (upper panel), the dark-yellow color of the sample prepared without Eu (reference) was attributed to a mixture of phases, with the features of the non-PSK δ-phase at low angles and a diagnostic peak of a PSK phase at $2\theta \approx 20.3^\circ$. Figure 2a represents a hypothetical fitting curve for δ+γ mix of phases (≈50% each) with lattice parameters of the black γ-phase reported in the second column of **Table 1**, and those of the δ-phase being $a = 10.421$ Å, $b = 4.604$ Å, $c = 17.873$ Å (refinement from the Pnma lattice structure reported in the study by Straus et al.^[22]). We notice that, for a better fit of the peak at $2\theta \approx 20.3^\circ$, the c axis should be increased from 12.380 Å toward the values reported in the literature (≈12.5 Å)^[21,22,29] with consequences that will be clear in the following discussion. In regard to the attribution of the peak at $2\theta \approx 20.3^\circ$ (α-, β-, or γ-phase), there are not enough details in the diffraction pattern (differently from the ones of powder and single crystals) to definitely decide (the layer is thin, and the composition is a mixture of black + yellow phases).

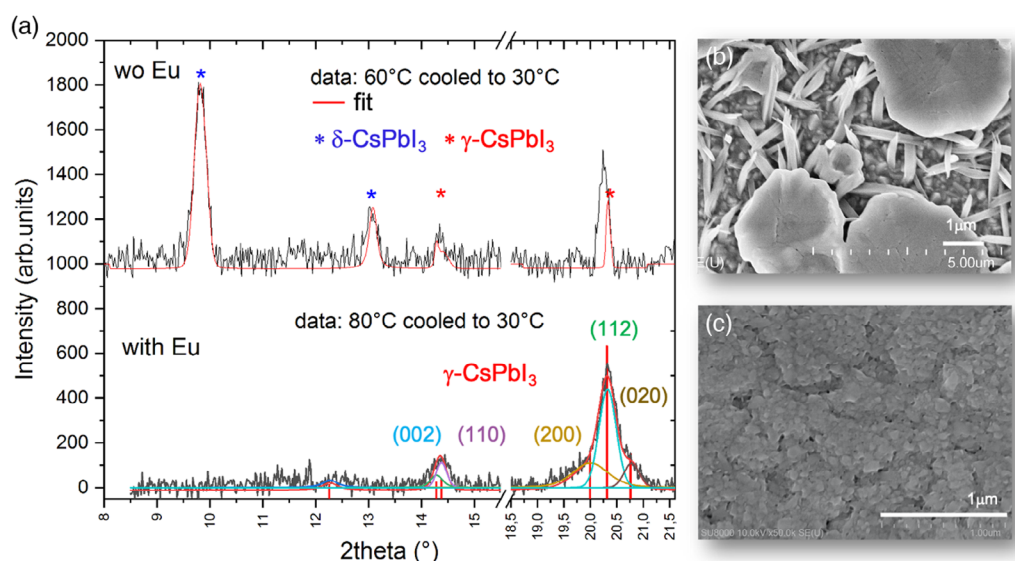


Figure 2. Structural and morphological analyses after quenching with and without using Eu precursors. a) The XRD patterns have different features depending on Eu presence: with Eu, an orthorhombic lattice structure is established that is fitted by a black γ -phase with lattice constants slightly modified with respect to references values^[21,22] (vertical red bars are markers of γ -phase planes with the labeled Miller indexes with lattice parameters $b < a < c$); without (wo) Eu, the material is a mixture of PSK and a non-PSK δ -phase (mixed material). The crystallographic grain size extracted by the full width at half maximum of the diffracted peaks is in the range 10–20 and 30–60 nm with and without Eu, respectively. b) SEM image of a mixed material without Eu, that accounts for the dark-yellow color of the sample. The elongated grains ($>1 \mu\text{m}$) are the yellow δ -phase. c) Monophase nanostructured PSK layer with grain diameter $<100 \text{ nm}$, as grown using Eu in the preparation procedure. This fine-grain structure is consistent with the use of a LT (80°C), while a γ -phase quenched from HTs, as done in previous studies,^[22,29] has large grains due to grain coalescence and ripening.

Table 1. Average lattice parameters and standard deviation measured on the thin layers with $\text{Eu/Pb} = 5\%$ prepared by spin coating on glass and on TiO_2/FTO substrates with respect to what reported in the literature for single crystals, powders, and thick layers after scratching.

Lattice parameters of the orthorhombic γ -phase [Å]	This work spin coated layers quenched from 80°C using Eu	Sutton et al. ^[29] powder fast quenched from 347°C in N_2	Marronnier et al. ^[21] powder quenched at 2.5 K min^{-1} from 370°C with N_2	Straus et al. ^[22] single crystals quenched from 370°C in iced water
Symmetry group	Space group 62	Pnam(62)	Pbnm(62)	Pnma(62)
a	8.855 ± 0.025	8.856	8.620	8.864
b	8.570 ± 0.032	8.577	8.852	12.484
c	12.380 ± 0.016	12.472	12.500	8.578

The black color of the layer prepared with Eu (Figure 1c) was invariant on different samples over glass as well as on TiO_2/FTO substrates and represents the first clue on the formation of a uniform PSK phase all over the sample surface. Different from the previous case, the related XRD pattern contains enough information to shed light on which PSK polymorphism is dominant in the layer. As shown in Figure 2a (lower panel), diagnostic peaks are found in the angular range $2\theta = 14\text{--}22^\circ$ whose position and shape were pivotal. It is particularly interesting that the feature with maximum at $2\theta \approx 20.3^\circ$ is a result of the superimposition of three peaks. They were deconvoluted (pseudo-Voigt shape) and ascribed to (200), (112), and (020) planes of the γ -phase. In this range, α - and β -phases would instead have only one and two peaks, respectively, and are indeed excluded. The complete fitting curve and parameters extracted by standard Rietveld refinement procedure can be found in the Supporting Information (S1).

Table 1 shows the average values of the measured parameters and the related standard deviations collected in different samples on glass and TiO_2/FTO .

Figure 2b,c shows the different morphologies of the two layers prepared without and with Eu, wherein we notice the double texture of the sample prepared without Eu (to be associated to a double-phase composition as found in the diffraction pattern) in contrast to the structural uniformity of the other sample (single phase in the diffraction pattern). This homogeneous fine-grained structure is consistent with the use of a low formation temperature (80°C), while γ -phases quenched from HTs, as done in the studies by Straus et al. and Sutton et al.,^[22,29] have large grains due to grain coalescence and ripening. To justify the fine structure and the γ -phase formation at low T using Eu, the formation of PbI_2 -dimethyl sulfoxide (DMSO) adducts^[33] was excluded to have a main role on the basis of the γ -phase instability without europium (same solvents used) demonstrated by XRD (see also the Ellipsometric results in Section 2.5).

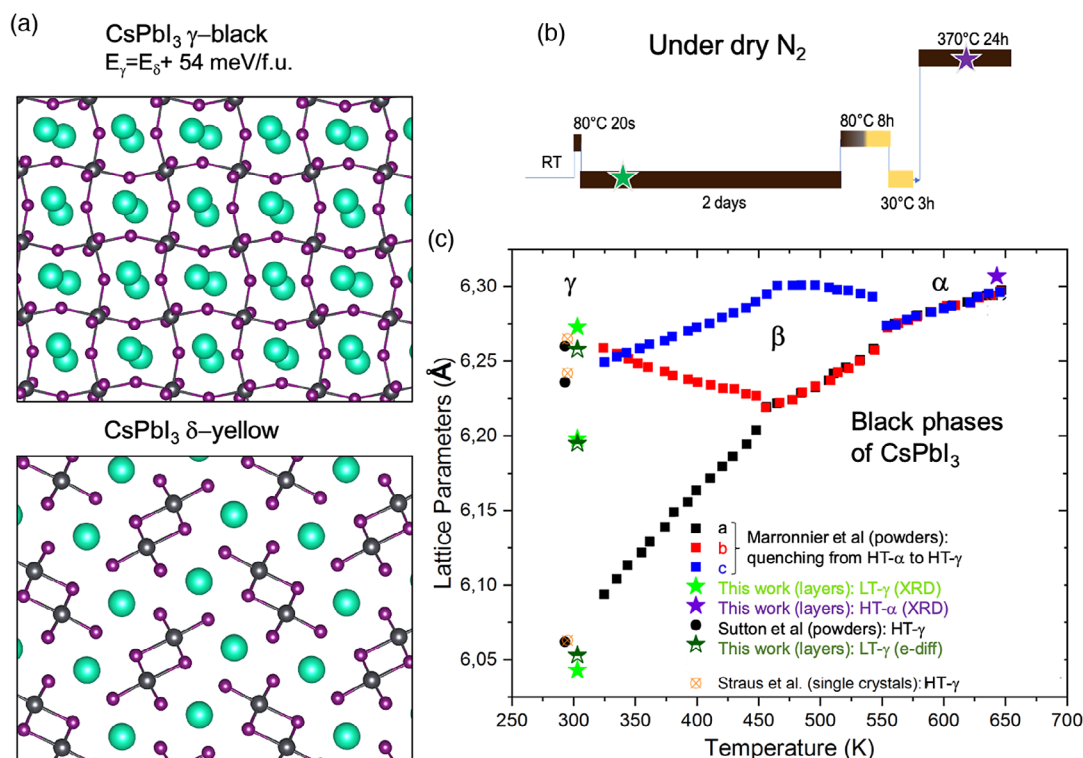


Figure 3. a) Optimized γ and δ structures based on DFT calculations projected on the (001) and (010) planes, respectively. The calculated ground-state energy (f.u. = formula unit) shows that the δ -phase is preferred with respect to the γ -phase in bulk systems and at LTs. b) In situ heating and cooling path used to extract c) the lattice parameters of the material, with special regard to what occurs after quenching from LT (80–30 °C: green stars) and at HT (370 °C) wherein a cubic α -phase is established (violet star). The pseudocubic lattice parameters of the PSK γ -phase formed using Eu and measured at room temperature are compared with literature data (see also Table 1). On this basis, we find that the black-LT γ -phase lattice has a c -value slightly but statistically smaller than the ones reported in the literature after quenching from HT (Marronnier et al.,^[21] Straus et al.,^[22] Sutton et al.,^[29]) In this respect, XRD and electron diffraction data are in full agreement.

Figure 3a compares the two orthorhombic lattices of the PSK γ -phase and non-PSK δ -phase with ground-state energies that are 54 meV apart per formula unit (i.e., 10.8 meV/atom, 216 meV/unit cell) based on density functional theory (DFT) calculations, remarking a spontaneous tendency to form the δ -phase in bulk materials. This description of the atomic arrangement in the two lattices denotes that shifting from one to the other implies a relevant reorganization and diffusion of species, with Cs as the biggest atom involved in the kinetics.

The overall thermal path sketched in the upper panel of Figure 3b is applied and the pseudocubic lattice parameters correspondingly extracted in the LT γ -phase and in the (HT) α -phase during XRD in situ analysis on a representative sample. The related data are shown in Figure 3c by colored stars. A peculiarity of the LT γ -phase prepared with Eu is the c -value (the longest axis) that is smaller than what reported for bulk materials, thick layers or powders quenched from HT or from 100 °C (see Table 1).^[21,22,29] The associated cell volume is consequently smaller by $\Delta V/V = -(0.7-1.4)\%$. We found a similar result by changing the precursor from EuCl_3 to EuI_2 as opposed to what we measured in the samples without Eu. As a matter of fact, the red fitting curve in Figure 2a (upper panel) does not match the peak at $2\theta = 20.3^\circ$ using a, b, c , as shown in the second column of Table 1. The detected peak is instead shifted leftward with the

c -axis that consequently moves to reference standard values around 12.5 Å. This important finding implies that the γ -phase formed without Eu in our thin layers is similar to the rest of the cases reported in the literature (see Table 1).^[21,22,29]

Moreover, we noticed that the c value measured on our film at RT closely matches a case^[22] measured at a temperature of 100 K ($b/2$) in that case. The other two reported lattice parameters at 100 K are instead stretched upward and downward with respect to what we measured. In that study, a double site occupancy for Cs was proposed: Cs_A (Cs in A site) and Cs_B (Cs in B site), with Cs_B being more centrally located in the polyhedron than Cs_A . It is there additionally shown that at 100 K the degree of Cs occupancy in the B-site is close to zero and the octahedral distortion is reduced (e.g., see the I–Pb–I angle as a parameter).^[22] A question that indeed arises is how Eu presence eventually acts on the octahedral coordination configuration and if this has an impact on the volume within the overall energy balance. This will be elucidated by DFT calculations in Section 2.4.

2.3. Interplay between Eu Incorporation and Morphology in the LT γ -Phase

We rise a second argument on the role of morphology, structure, and local composition of the LT γ -phase. Pivotal insights are

gained through transmission electron microscopy (TEM) analyses with associated electron diffraction for phase identification and local chemical probes for electron energy loss spectroscopy (EELS) and energy dispersive X-ray spectroscopy (EDX) analyses. For this investigation, the samples were dispersed on a carbon-coated Cu grid by spin coating that avoided using standard mechanical preparation procedures.

Figure 4a,b shows a mixture of small rounded grains of the γ -phase and elongated grains of the δ -phase formed in the reference sample without Eu and identified through electron diffraction (SI2), in agreement with XRD and scanning electron microscopy (SEM) findings (glass or TiO₂/FTO substrates used). In contrast, in the sample prepared with Eu, a uniform monodisperse layer made of small grains is found (Figure 4c) and univocally attributed to the orthorhombic γ -phase through electron diffraction analyses such as the ones shown in Figure 4d (large-area diffraction pattern) and Figure 4e (selected area diffraction pattern). We notice that the lattice parameters evaluated

through those patterns (dark-green stars in Figure 3c) approach the values found by XRD, with the c -axis smaller than the ones reported in the literature (see Table 1).

As another important finding, we observe that the grains of the γ -phase are surrounded by a shell of material (intergrain region) that creates an interconnecting gluing network (Figure 4c). This thin intergrain region, a few nanometers-large, looks brighter with respect to the grains as it has thickness and/or composition different with respect to the grain core. As a matter of fact, the EELS spectra taken inside this networking material unveil the presence of Eu together with Cs and I species, as shown in Figure 4f (light-blue line). The red spectrum is instead acquired as a reference inside a PSK grain. The lack of signal from Eu in this spectrum does not necessarily imply that Eu is not present in the grain core because the EELS sensibility is limited to few atomic percent. Hence, it rather states that the content of Eu inside the grain is less than 1–2 at%. A closer inspection on the shape of the EELS spectrum of europium taken

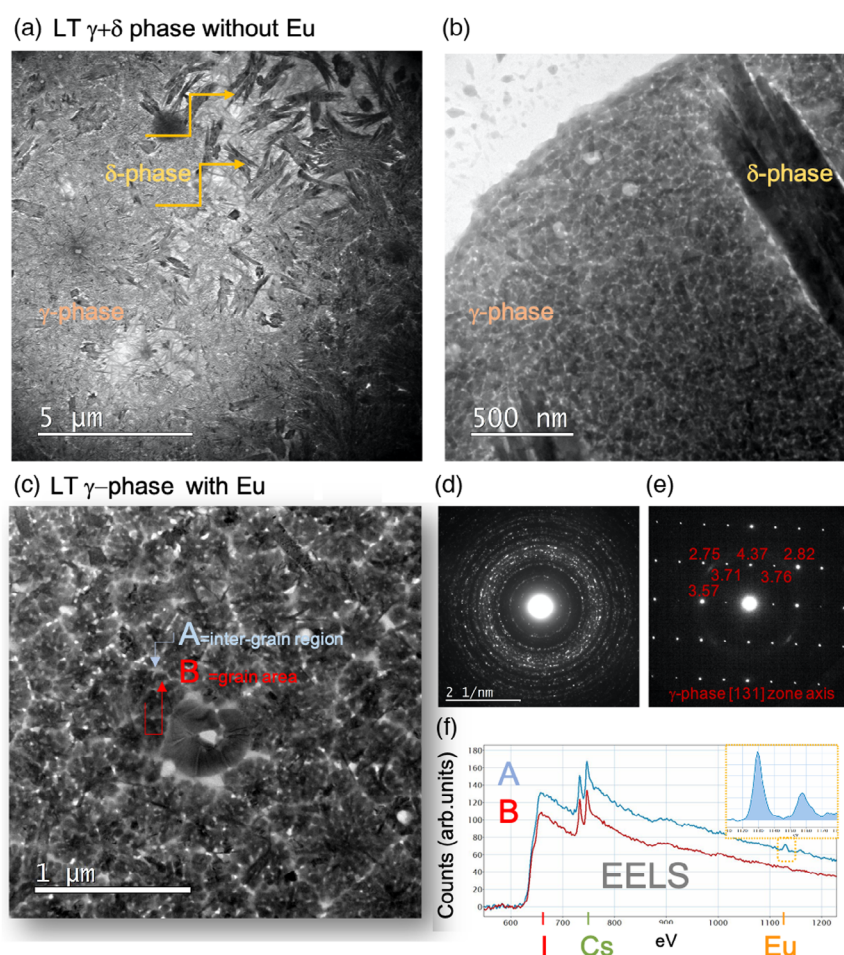


Figure 4. a,b) Plan-view TEM images of the LT $\gamma + \delta$ -mixed material prepared without Eu characterized by rod-like grains (δ -phase) and rounded grained (γ -phase) as further shown in SI2, Supporting Information. c) Plan-view TEM image of the LT γ -phase prepared with Eu and characterized by small grains, 5–20 nm in diameter, radially arranged in larger aggregates. An intergrain material is also found. d,e) Electron diffraction patterns taken over large and selected areas that describe a pure γ -PSK lattice. The large density and specific location of the many diffraction rings in the large-area diffraction pattern unequivocally denotes the orthorhombic nature of the lattice. Specific interplane distances are labeled in orange (numbers are in Å) in the selected-area diffraction pattern and the related zone axis is also indicated, all diagnostic of an orthorhombic γ -phase. f) EELS indicating that Eu takes part to the material, especially at the grain boundaries. The inset is the detail of the europium spectrum that fits the one of Eu²⁺ as reported in the study by Li et al.^[33]

at the boundary of the grains and compared with spectra reported in the literature such as in the study by Mundy et al.,^[34] has highlighted that Eu^{2+} charge states are mostly established inside the sample (inset in Figure 4f). This finding implies that Eu gains the 2+ state during reaction whatever the initial charge was in the mother solution (3+ in the solution containing EuCl_3) and that the detected charge state accounts for the established coordination in the solid state.

We then proceeded with a spatial-resolved chemical analysis to unveil the local composition of the layer. For this purpose, we exploited the fact that the LT γ -phase prepared with Eu partially and slowly transforms into the δ -phase over long aging times. Although the transformation was not as fast as in the case without Eu (see Section 2.5), partial degradation can be reached that leaves the two phases coexisting on the same sample. This mixed composition allowed performing simultaneous investigations of two phases in a same sample using scanning transmission electron microscopy (STEM) and EDX analyses.

Typical probed areas are shown in Figure 5a,b representing δ -phase and LT γ -phase regions, respectively, taken via STEM on the same sample. We used the relative percentage of Cs/Pb and Eu/Pb measured by EDX to discriminate the composition of the γ -grains from the composition at the intergrain regions (Figure 5c). A representative EDX spectrum taken in the intergrain region is shown in Figure 5d: it contains I, Pb, and Cs intense peaks and a small Eu peak. This is a second direct evidence about Eu taking part in the PSK layer. Further insights in this respect are paramount to understand its role.

On the basis of data in Figure 5c, we draw preliminary conclusions as follows: 1) the grains of the γ -phase prepared with Eu have an average content of Eu slightly above the threshold of detectability, with the benchmark represented by the CsPbI_3 γ -phase that did not contain Eu in the mother solution (wo Eu in Figure 5c); 2) associated with this, a relative deficiency of Cs with respect to Pb content is found in the γ -grains with Eu; 3) the Eu/Pb ratio in the intergrain region settles around 5–10%, with the upper limit associated to regions with Pb deficiency rather than with Eu over stoichiometry (e.g., $\text{Eu/Pb} = 0.15/0.85$, see caption of Figure 5). The Cs or Pb deficiency shown by our EDX measurements could also imply an improved energetic equilibrium between the PSK and the yellow phase, which can aid in the stabilization of the former.^[35] Together with this, a large dispersion of values on the Cs content has been found denoting a nonuniform distribution of species (and composition) in the intergrain regions. In particular, Cs abundance was occasionally found associated with Cl (e.g., $\text{Cl/Cs} = 29/9$), but this set of data was intentionally excluded from the data representation in Figure 5c (see Figure S3, Supporting Information) to make the intergrain comparable with the core regions wherein Cl was never found.

All those findings imply two main consequences: 1) Eu is mostly pushed outside the grains during formation; 2) part of the initial amount, around or even under 1 at%, can be left inside or at the grain periphery, substituting Pb or in other (e.g., interstitial) positions.

This last scenario would be compatible with a local compensation of charge between Eu (addition) and Cs (depletion) cations. The excess of Cs, as shown, stays in the intergrain space. Among the possible reason why Cs is less prone to enter the

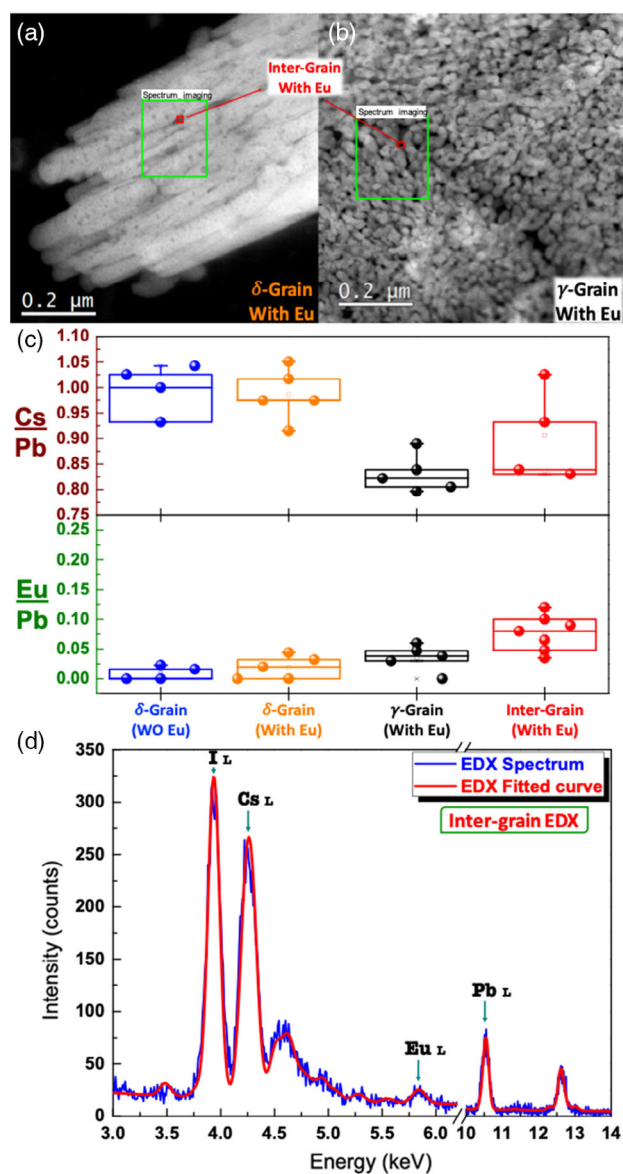


Figure 5. Dark-field STEM images of a) δ -phase grains, b) γ -phase grains of the CsPbI_3 sample taken on the same sample. The green box indicates typical probed region by EDX mapping (each pixel contains a spectrum; pixel size $\approx 2 \text{ nm}^2$), while the small red boxes indicate the intergrain region in both PSK phases. c) Statistical study of the cations ratio (Eu/Pb and Cs/Pb) in the different regions of the same sample (δ -grain, γ -grain, and inter-grain) with Eu compared with the reference case, i.e., the δ -grain without Eu (wo Eu). Each spot inside the box plots is the sum of different spectra (10–12 at least) of the respective probed region taken over an area as large as $800 \times 800 \text{ nm}^2$. d) A representative EDX spectrum taken in the intergrain region and the related fitted curve, with labeled the emission edges (L) of the species (I, Cs, Eu, and Pb) assigned to the peaks. The intergrain region has not a uniform composition and is mostly amorphous. We note that in the data representation: 1) the Cs/Pb boxplot does not include grains with Cs–Cl abundance (e.g., $\text{Cl/Cs} = 29/9$); 2) the Eu/Pb ratio can be locally above 5% due to Pb deficiency (e.g., $\text{Eu/Pb} = 0.15/0.85$) rather than to Eu over stoichiometry.

lattice, we include the large size of Cs and the presence of small Cl anions that are kinetically competitive to I in the interaction

with Cs during the reaction process. As a matter of fact, Cs and I have been preferentially found together in some intergrain regions, both relatively more abundant with respect to the other species.

We additionally found that, similarly to the case in which EuCl_3 is added in the mother solution, a γ -monophase made of small-sized grains glued by an intergrain network (Figure S4, Supporting Information) is formed when 5 at% EuI_2 (with respect to the stoichiometric CsPbI_3) is used.

All those findings lead us to generalize that exceeding (together with slower) species are progressively accumulated by a snowplow process toward the grain periphery during grain growth and consequently create a gluing network of self-material (i.e., species that in principle could take part to the PSK lattice structure, without additives of different nature) among the grains. Its presence has a role in retaining the small grain size by likely reducing the growth rate and/or inhibiting ripening and coalescence processes. The phenomenon could also be at the root of the use of HI additives that produces small CsPbI_3 γ grains, as reported in the study by Sutton et al.^[29] A similar size effect with a gluing network is exploited in the literature to stabilize CsPbI_3 α -phase nanograins by colloidal synthesis.^[36] Size-related effects for the γ -phase are also extensively discussed in the study by Zhao et al.^[37] In all reported cases, likewise in our case, the

interplay between surface energy costs and volume energy gain is the cornerstone to extend the lifetime of PSK CsPbI_3 phases.

Our next purpose is disclosing how Eu takes part and/or promotes the described layer structure with the consequent stabilization of the γ -phase. The phenomenological description is, in this respect, enriched by the data in Figure 6.

Figure 6a shows a high-resolution high-angle annular dark-field (HAADF)-STEM image of small grains whose core is well ordered (crystalline lattice). It is made of rows of aligned atoms that are distinguished on the basis of the location of Pb or Cs together with iodine species (zone axis [1–12]). The related fast Fourier transformation (FFT) together with the lattice reconstruction univocally identify the γ -phase of CsPbI_3 without any byproduct. An outer shell is also visible in the HAADF-STEM image wherein the lattice order is less defined or even lost. Spatial-resolved EDX analyses in Figure 6b, mediated over 32 spectra ($4 \times 4 \text{ nm}^2$ each) and taken in the three regions (grain core, grain shell, and intergrain), shows that Eu is mostly distributed along the grain shell wherein the lattice order is reduced with respect to the ordered crystalline grain core. Those boundaries create an interconnective tissue from one grain to another above a background region (darker in the image) that we called snowplow self-material. It collects species such as Pb, I, Cs, and Eu, as shown in Figure 5 (intergrain region), with the addition of

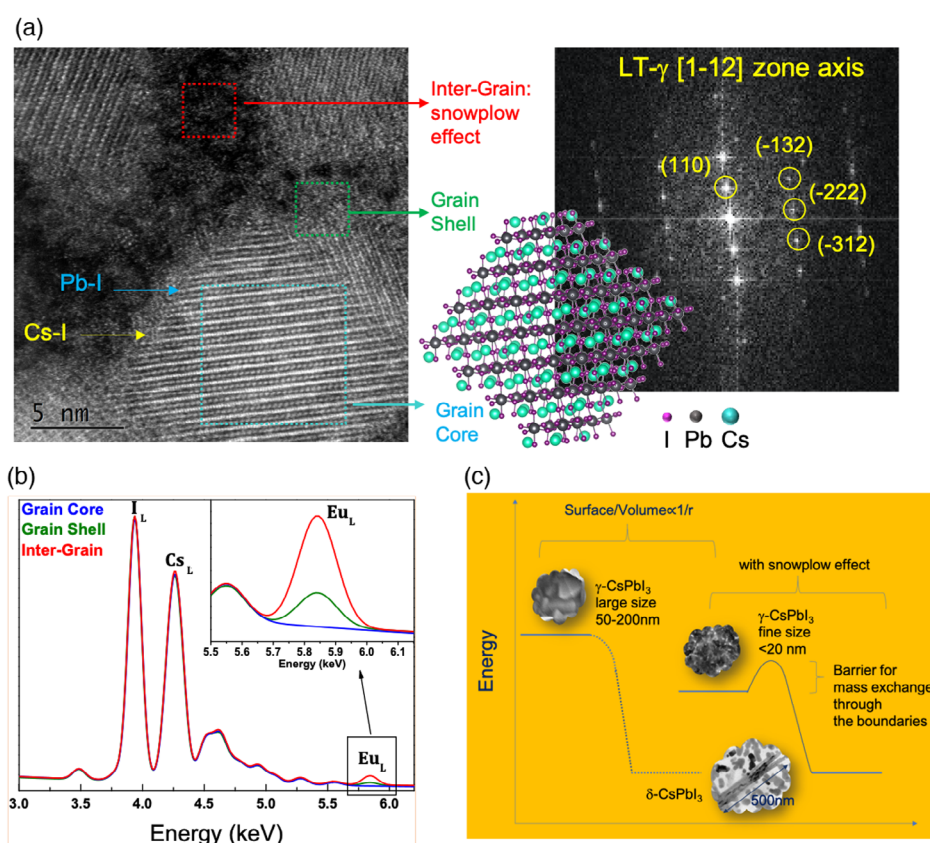


Figure 6. a) HAADF-STEM image of small grains in the γ -phase framed by a gluing matrix of self-material. The related atomic configuration and FFT are correspondently shown in the right panel. b) EDX spectra taken in the three regions labeled in (a). c) Representation of the surface-to-volume energy interplay for this fine-grained morphology that is in favor of the γ -phase in contrast with the case of larger grain morphologies (e.g., without Eu). In the first case, a kinetic barrier has to be overcome to allow the phase transition toward the δ -phase.

Cl. In this intergrain region, abundance of Eu and/or deficiency of Pb is found. We additionally note that the composition of this snowplow material is not uniform, with Cl and Cs often more abundant in some locations (Figure S3, Supporting Information). This result confirms that Cs diffusion during reaction compete with Cs–Cl interaction/reaction. It likely causes Cs deficiency at the grain boundaries wherein Eu can compensate the positive lack of charge by establishing iodine bonding together with Pb in a distorted (amorphous) arrangement. We could even argue that the other way around or that both phenomena are acting, namely less Cs participating to the reaction and Eu coordination with iodine in a distorted CsPbI₃ matrix synergically cooperate.

Further CsPbI₃ grain growth is inhibited by the presence of the intergrain frame. The retention of this fine-grained γ -phase during time after reaction (i.e., after quenching from 80 to 30 °C) occurs due to a convenient balance between the surface energy cost (in favor of the γ -phase) and the bulk energy gain (in favor of the δ -phase). In this complex scenario, Eu primarily serves to locally balance the missing charge. As a second effect of this small-grain configuration with the intergrain gluing self-material, a kinetic barrier to move LT γ -phase to δ -phase is established to upset the atomic arrangement. All those effects are shown in Figure 6c. As an additional positive achievement, the small size of the grains with their damping intergrain shell provides the lattice with a degree of “octahedral flexibility” that allows maintaining a slightly distorted lattice (*c*-reduction as measured by XRD) for a better accommodation of the γ -phase.

2.4. DFT Calculations for the Interpretation of the Role of Eu

Based on the experimental evidence, we carried out DFT calculations to investigate if the presence of Cs vacancies, related to the experimentally observed Cs deficiency, along with the

introduction of Eu interstitials changes the electronic characteristics of the CsPbI₃ PSK at the bandgap region near the grain shell. This aspect is important as it clarifies if Eu²⁺ cations, upon the hypothesis that they do not solely substitute Pb²⁺, introduce electronic states which are detrimental for the operation of PSK solar cells. We approximated the EDX stoichiometric data (Figure 5c) by considering orthorhombic CsPbI₃ supercells having a 12.5% of Cs vacancies and 6.25% of Eu adatoms, where Eu²⁺ occupies vacant spaces left from the deficiency of Cs⁺. The resulting system is a Cs_{0.875}Eu_{0.0625}PbI₃ alloy. We developed different configurations that correspond to this stoichiometry (see Figure S5, Supporting Information) and investigated if the configurational variability also reflects different structural and electronic properties for the system. Upon structural relaxation of the atomic positions and the lattice parameters, we noticed that all configurations shared the following characteristics: a) the PSK lattice was preserved notwithstanding the high concentration of defects and impurities; b) the volume of the Cs_{0.875}Eu_{0.0625}PbI₃ alloy was smaller than the volume of the ideal CsPbI₃ PSK due to the smaller ionic radius of Eu²⁺ with respect to Cs⁺ along with the presence of Cs vacancies. Such volume contraction agrees with the XRD data of Figure 2 and Table 1; c) in all configurations the Eu²⁺ cation formed an octahedral EuI₆ network with neighboring I[−] atoms (see Figure 7a), in agreement with the shape and position of most of the EELS spectra of europium (Figure 4f). This evidence is important as it implies that Eu, once integrated within the solid-state PSK lattice, forms bonds with iodine anions by preferring the 2+ oxidation state.

Hence, Eu-centered octahedra share the same apical iodine atoms with Pb-centered octahedra. We point out that the EuI₆ octahedra are rather distorted with their I–Eu–I angles significantly deviating from the ideal 90° value. To understand if this cation mixing can give rise to deep-level states within the CsPbI₃ bandgap, we calculated the density of states for the alloy

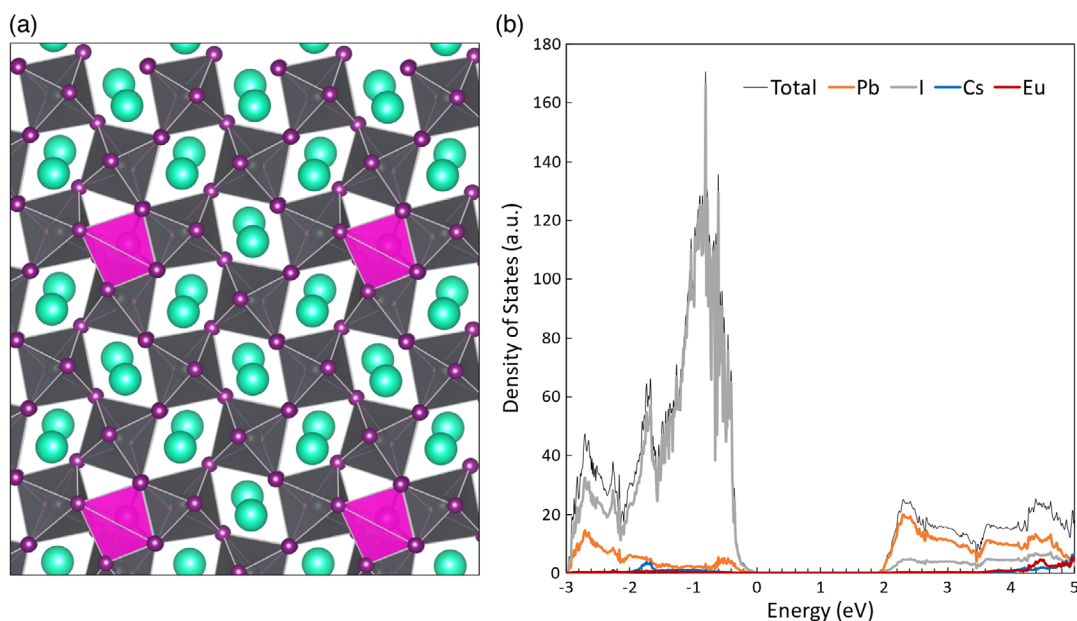


Figure 7. a) Schematic representation of a Cs_{0.875}Eu_{0.0625}PbI₃ alloy, where Pb-centered octahedra (gray) share the same apical iodine atoms with Eu-centered octahedra (violet). b) Density of states as a function of energy for the Cs_{0.875}Eu_{0.0625}PbI₃ alloy shown in (a).

configuration that has the lowest formation energy within the studied configurations (Figure S5a, Supporting Information). Results showed that the electronic states deriving from Eu atoms are outside the bandgap and far from the band edges (Figure 7b). It is interesting to note that each Eu^{2+} cation in this system efficiently compensates two Cs^+ vacancies, maintaining the overall charge level of the system unchanged. Therefore, no deep-level states were observed within the bandgap area, showing that Cs deficiency along with the addition of Eu during the growth process do not significantly modify the intrinsic optoelectronic properties of the CsPbI_3 crystal, even at the defected grain peripheries.

2.5. LT γ -Phase Endurance

The kinetic change from LT γ -phase to δ -phase has been investigated by in situ experiments using spectroscopic ellipsometry technique to explore the endurance of CsPbI_3 samples with Eu in comparison with the ones without Eu. In these latter samples, similar to what was found by XRD (Figure 2), a mixture of LT γ -phase and δ -phase is unavoidably formed as attested by features in the dielectric function.

In **Figure 8**, we show the imaginary part of the dielectric function for CsPbI_3 samples with and without Eu measured at 30 °C after formation at LT (80 and 65 °C, respectively) and after post-formation annealing.

The dielectric function has been obtained from modeling the spectroscopic ellipsometry data.^[15,38] The LT γ -phase of CsPbI_3

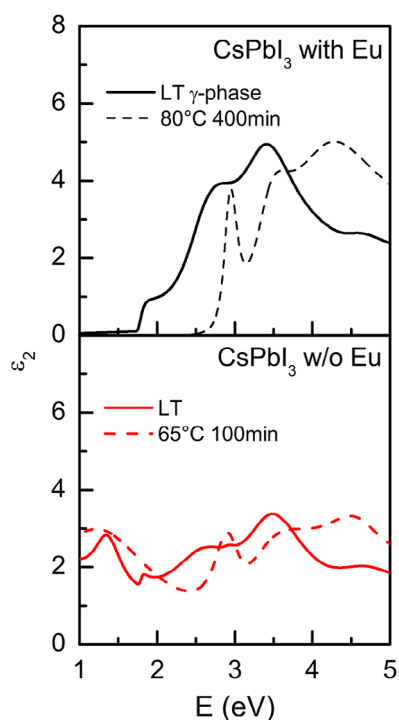


Figure 8. Imaginary part of the dielectric function as obtained from spectroscopic ellipsometric measurements on CsPbI_3 with Eu and without Eu after formation at LT (80 and 65 °C, respectively) and subsequent quenching to 30 °C compared with data after postformation annealing and quenching to 30 °C.

with Eu has a negligible absorption inside the bandgap (below 1.7 eV) indicating the absence of defects contributing into the gap. Similarly, in the δ -phase formed after postreaction annealing at 80 °C for 400 min, we do not observe states inside the gap that has consistently moved to 2.7 eV. In contrast, the sample without Eu shows in both cases (after formation and after post-annealing), an intense absorption under E_{gap} attesting that a broad band of defects exists inside the gap.

A quantitative understanding of the previous data from the point of view of allowed interband energy transitions is possible thanks to the critical point (CP) analysis.^[15,39] This analysis relies on the singularities in the electronic densities of states corresponding to CPs in the dielectric function.^[40–43] These points are identified by calculating the second derivative of the measured dielectric function (Figure 8) and fitting simultaneously the real and imaginary parts using a least-squares procedure with the following equation

$$\frac{\partial^2 \epsilon}{\partial \omega^2} = n(n-1)Ae^{i\Phi}(\omega - E + i\Gamma)^{(n-2)} \quad (1)$$

where E , Γ , A , Φ , and n (n different from Φ) describe the shape (energy threshold, amplitude, broadening, excitonic phase angle, and singularity dimension, respectively) of the dielectric function around each transition point. The LT γ -phase is characterized by CPs at 1.78 eV (the gap, that is not modified by Eu), 2.58 and 3.37 eV, whereas the δ -phase is characterized by CPs at around 2.95 (the gap) 3.36, and 4.3 eV. The two phases share a CP around 3.36–3.37 eV.

We determined the stability extent of the LT γ -phase with Eu by increasing the temperature from 30 °C to a set of values (80, 90, or 100 °C). During the isothermal annealing (see representative measurements at 80 °C in **Figure 9a**) the CsPbI_3 with Eu sample slowly transforms into the δ -phase.

When the same approach was used in the sample without Eu, the transformation was so rapid that we were forced to work at only 65 °C to have sufficient time to carry out the ellipsometric measurements (see **Figure 9b**) and appreciate the transformation. According to this, solar cells without Eu have poor characteristics, whereas the ones with Eu can be measured and characterized, as shown in the study by Jena et al.^[27] and **Figure S16**, Supporting Information. Thanks again to the CPs analysis, we established a precise time scale of the phase transition for each material. To this scope, among all CPs, we show only the most significant ones at the energy gap of the LT γ -phase (≈ 1.78 eV) and the energy gap of the δ -phase (2.95 eV) (see **Figure 9c,d**).

From that analysis we concluded that: 1) with Eu, the absorption onset (E_{gap}) of the LT γ -phase around 1.8 eV has a blue shift and decreases in amplitude during the isothermal cycle. When this point reaches the value of 1.83 eV, its amplitude becomes zero (i.e., complete disappearance) because the sample is fully transformed in the δ -phase. This transition takes 400 min at 80 °C; 2) with Eu, the degradation process from γ to δ -phases has a temperature-dependent incubation time (100 min at 80 °C) in which the gap of the γ -phase remains constant (and this roughly corresponds to the absence of the δ -phase or to its very early nucleation); 3) the phase transition from γ to δ phases

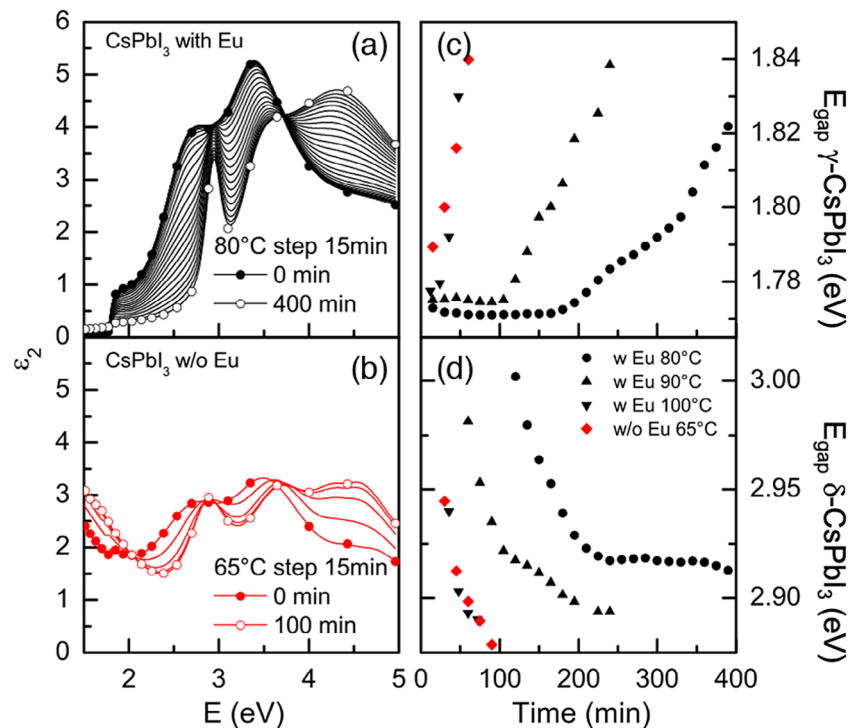


Figure 9. Imaginary part of the dielectric function of CsPbI₃ a) with Eu and b) without Eu during isothermal annealing at 80 and 65 °C, respectively. Time dependence of E_{gap} of the LT c) γ -phase and d) δ -phase of CsPbI₃ with Eu (black lines) and without Eu (red lines) for different temperatures.

occurs in the same time scale at a temperature of 100 °C using Eu and at 65 °C without Eu, that is with 35 °C of gain in stability.

Using the same calculation of the E_{gap} by the CP analysis, **Figure 10** shows how the energy gap of the LT γ -phase (with Eu) moves with temperature while the sample is cooled under RT step by step. A continuous trend of E_{g} that reduces with T is found down to -100 °C, with the γ -phase preserved. As a second important finding is that the initial value of E_{g} is fully recovered after T was getting back to 30 °C.

The data in Figure 10 extend what is already known on the continuous and reversible structural behavior of the γ -phase of CsPbI₃ below RT^[22] by demonstrating that the optical bandgap is also reversibly recoverable. As a step beyond, it suggests that the two possible thermally activated Cs positions found in the study by Straus et al.^[22] are reversibly occupied by changing the temperature, and particularly moving below and reapproaching again room temperature. Based on ellipsometric data and according to the study by Straus et al.,^[22] we argue that the

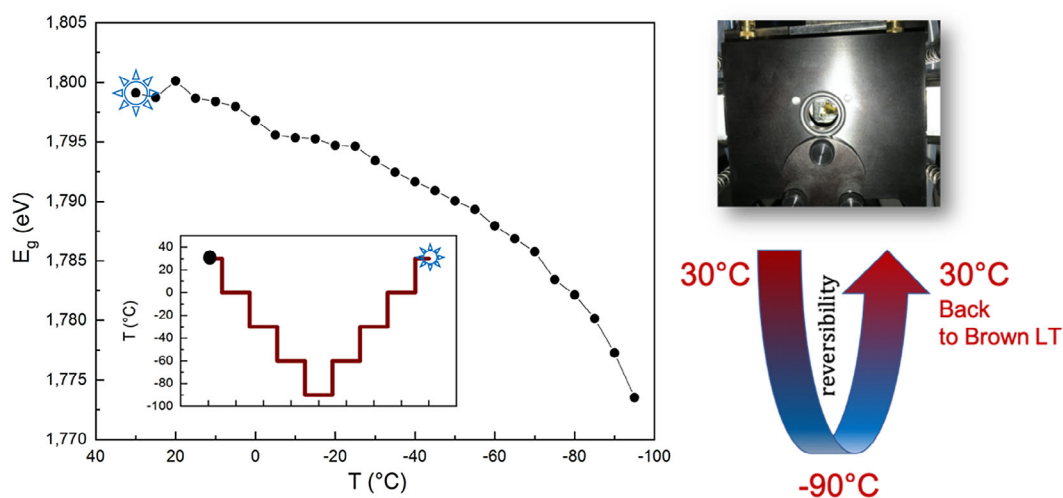


Figure 10. Gap behavior and its full recovery after cooling down in CsPbI₃ with Eu samples that show the stability of the optical response of the material.

LT γ structure^[15] with its I–Pb–I bond angles^[30] elastically and reversibly move during the back and forth temperature pathways.

3. Conclusion

A purely orthorhombic γ -phase of CsPbI₃ was established at 80 °C equivalently on glass as well as on TiO₂/FTO substrates using 5% atomic ratio between Eu and Pb in the mother solution. This was stabilized at 30 °C by a simple quenching procedure and called LT γ -phase. The procedure comprises a spin-coating step followed by a heating to 80 °C cooling to 30 °C procedure at rate of $\approx 0.5\text{--}1\text{ }^\circ\text{C s}^{-1}$ in dry-N₂ environment. The resulting layer is made of nanograins with diameter in the range 5–20 nm, interestingly separated by an intergrain matrix holding the PSK phase network. When compared with a similar layer prepared without Eu, that is initially a mixture of LT γ -phase and a predominant δ -phase of CsPbI₃, the sample with Eu in its pure LT γ -phase exhibited a hugely longer lifetime in the range 65–100 °C.

The structural features of that sample in the LT γ -phase, disentangled through a combination of advanced analytical techniques coupled with DFT calculations, evidence multiple roles played by Eu with a common thread that could be further extended to the use of other additives.

It has been found that only part of the available Eu amount is incorporated into the nanograins of the LT γ -phase. In addition to Eu that replaces Pb, Eu atoms also occupy interstitial sites in the orthorhombic γ -phase establishing distorted sixfold coordination with iodine species. This configuration agrees with our finding on a Cs-deficient stoichiometry, with Eu compensating the local charge in the lattice. This consequently leads to cell volume contraction, which is consistent with experimentally measured 1–2% contraction of the cell volume, also supported by DFT calculations.

The Cs–Eu–Pb interplay in the atomic arrangement is compatible with the existence of an outer grain shell wherein the ideal lattice order is lost and distorted atomic arrangement becomes accessible or even convenient. As a matter of fact, an intergrain transition region is found wherein the overall composition deviates from the one at the grain cores. In the composition, excess of Eu is the main finding indicating that, in the growth process, part of the host atoms is incorporated, whereas the rest is displaced through a snowplow effect, i.e., a kinetic process that tends to accumulate Eu atoms toward the outer part of the grains. As a further kinetic effect, abundance of Cl and Cs is found at the intergrain region. The exceeding material (with local unbalanced stoichiometry) creates a barrier that inhibits a further increase in the grain size. This, in the end, allows keeping high the surface-to-volume ratio that is known to be beneficial for the γ -phase to be stabilized against the non-PSK counterpart in the δ -phase.^[44] The narrow intergrain frame has a further valence in retarding mass exchange and in prolonging the γ -phase stability.

The gained insights have a more general valence as benchmark to engineer self-materials through snowplow methods at LTs able to frame and freeze pure fine-grained structures of black CsPbI₃ phases. Charge compensation of cation deficiency is also encouraged in the preparation recipe. Our findings concurrently pave the way to further extend the black-phase stability at room temperature for more reliable solar cells.

4. Experimental Section

PSK Film Fabrication: A solution of 1 M PbI₂ (Tokyo Chemical Industry) and 1 M CsI (Tokyo Chemical Industry) was prepared by mixing them in a composite solvent made of dimethylformamide (DMF) and DMSO (3:1 v/v). EuCl₃ (Sigma-Aldrich) solution of 0.1 M concentration was made in same mixed solvent of DMF and DMSO (3:1 v/v). The solutions were stirred at room temperature for 1 h. Then, 1 mL of the PbI₂/CsI solution was mixed with 0.5 mL of the EuCl₃ solution to reach the desired stoichiometry and then stirred for 1 h. The PSK film was deposited by spin coating the precursor solution on glass substrates in two steps: 1000 rpm for 10 s followed by 5000 rpm for 25 s in ambient environment. The CsPbI₃ with Eu/Pb = 5% film was then annealed at 80 °C on a hot plate for 20 s and cooled to 30 °C at $0.5\text{--}1\text{ }^\circ\text{C s}^{-1}$ to form the LT γ -phase. The final layer on glass had a thickness of ≈ 80 nm. The composition of the mother solution was chosen according to the results of the study by Jena et al.,^[27] based on the best solar cell performances achieved.

X-Ray Diffraction: XRD patterns were collected using a D8Discover (Bruker AXS) diffractometer equipped with a high-precision goniometer (0.0001 Å), a thin film attachment (long sollar slits), and a Cu K α source (instrumental broadening 0.07°). An Anton Paar heating stage was used for in situ experiments equipped with a polyether ether ketone dome to keep the samples at controlled temperatures in controlled atmospheres. The temperature values (measured by a thermocouple) were crosschecked using commercial thermostrips (Raceteck-Thermal indicator strips) and were consequently given with an error bar of ± 1 °C. In situ XRD analyses were carried out in air or nitrogen, which were used to fill the dome at a pressure slightly above the atmospheric one (+0.3 bar). During cycles, the acquisition time corresponded to the use of a step size of 0.01° and acquisition time 1 s per step. After the sample was raised up to a temperature, the alignment procedure was repeated to consider the thermal expansion of the sample and of the silver paste used to increase the heating exchange.

Spectroscopic Ellipsometry: We used a V-VASE, J. A. Woollam spectroscopic ellipsometry for optical characterization. Ellipsometric data were collected at different angles below and above the Brewster angle of the glass substrate, over a wide range of wavelengths 245–1240 nm (1–5 eV) with step of 10 nm or less depending on the curve steepness. Then we built a Kramers–Kronig consistent optical model based on multiple Tauc–Lorentz oscillators to determine the real and imaginary parts of the dielectric function. Measurements were collected using a N₂-filled chamber to prevent PSK degradation in air. The cell setup allowed to vary the temperature in the range 30–325 °C with an Instec MK100 heater/cooler system with an accuracy of 0.1 °C.

Scanning Electron Microscopy, STEM, EDX, and EELS analyses: The morphology of the CsPbI₃ layers was checked with a scanning electron microscope (SU8000, HITACHI).

STEM analyses were carried out with a Cs-corrected JEOL ARM200C at 200 keV, equipped with GATAN Quantum EELS and JEOL energy dispersive X-ray spectrometer (EDXS). High-resolution images were acquired in scanning mode using the HAADF signal. Spectrum images were obtained with parallel HAADF, EELS, and EDXS acquisition. All the data analysis and elemental quantification were carried out with Gatan Microscopy suite v3.01. TEM samples were prepared via spin coating and annealing over a carbon-coated TEM grid directly stacked on a standard glass substrate. After annealing, the sample was quickly transferred to the TEM holder and introduced in the vacuum chamber. For TEM analyses, we initially used a low dose rate ($\approx 1\text{--}10\text{ e}^-/\text{Å}^2 \times \text{s}$) to settle a safe electron beam conditions but progressively we increased that value ones verified that the material was not damaged under prolonged acquisitions. The dose rate finally used was in the range $(1\text{--}10)10^4\text{ e}^-/\text{Å}^2 \times \text{s}$.

DFT calculations: DFT calculations were carried out with the Quantum espresso code^[45] using the Perdew–Burke–Ernzerhof^[46] exchange-correlation functional and ultrasoft pseudopotentials. To reproduce the experimental stoichiometry observed through the EDX measurements, we considered a $(2 \times 2 \times 1)$ CsPbI₃ orthorhombic supercell having a 12.5% of Cs vacancies and 6.25% of Eu adatoms. Three different configurations of the resulting Cs_{0.875}Eu_{0.0625}PbI₃ alloy were considered

(see Supporting Information) and the electronic properties were calculated only for the system having the minimum energy configuration (Figure S5a, Supporting Information). Convergence was achieved with a plane-wave cutoff kinetic energy of 49 Ry and an augmented charge density cutoff of 258 Ry. The supercells comprised 79 atoms, whereas equilibrium atomic positions and lattice parameters were obtained by an unconstrained variable-cell optimization of the structure. A $(4 \times 4 \times 6)$ Monkhorst–Pack grid^[47] was used for the sampling of the Brillouin zone. The VESTA software^[48] was used for visualization.

Supporting Information

Supporting Information is available from the Wiley Online Library or from the author.

Acknowledgements

A.A., E.S., and I.D. contributed equally to this work. The project was partially supported by the bilateral project on PSK Solar Cells (CUP B56C18001070005), cofounded by CNR (Italy) and JSPS (Japan). CNR gratefully acknowledges the project PON entitled “Tecnologia per celle solari bifacciali ad alta Efficienza a 4 terminali per utility scale,” called BEST-4U, financed by the Italian Ministry MIUR (CUP B88D19000160005) and the Project PON ARS01_01007 entitled EleGaNTe Electronics on GaN-based Technologies (CUP B91G18000200005). Computer resources were provided by the Swiss National Supercomputing Centre (CSCS) under Projects ID s869 and s963. The authors thank Prof. Stefan Goedecker from University of Basel (CH) for its valuable support.

Conflict of Interest

The authors declare no conflict of interest.

Data Availability Statement

Data sharing is not applicable to this article as no new data were created or analyzed in this study.

Keywords

delta phases, gamma phases, perovskites, phase transitions, stabilities, thin films

Received: April 6, 2021

Published online:

- [1] A. K. Jena, A. Kulkarni, T. Miyasaka, *Chem. Rev.* **2019**, *119*, 3036.
- [2] A. Alberti, E. Smecca, S. Sanzaro, G. Mannino, I. Deretzis, A. La Magna, *Riv. Nuovo. Cimento.* **2019**, *42*, 301.
- [3] I. Deretzis, E. Smecca, G. Mannino, A. La Magna, T. Miyasaka, A. Alberti, *J. Chem. Phys. Lett.* **2018**, *9*, 3000.
- [4] A. Alberti, I. Deretzis, G. Mannino, E. Smecca, F. Giannazzo, A. Listorti, S. Colella, S. Masi, A. La Magna, *Adv. Energy Mater.* **2019**, *9*, 1803450.
- [5] A. Alberti, I. Deretzis, G. Mannino, E. Smecca, S. Sanzaro, Y. Numata, T. Miyasaka, A. La Magna, *J. Phys. Chem. C* **2017**, *121*, 13577.
- [6] A. Alberti, C. Bongiorno, E. Smecca, I. Deretzis, A. La Magna, C. Spinella, *Nat. Commun.* **2019**, *10*, 2196.
- [7] P. Schulz, D. Cahen, A. Kahn, *Chem. Rev.* **2019**, *199*, 3349.

- [8] H. Chen, S. Yang, *Adv. Mater.* **2017**, *29*, 1603994.
- [9] S. Valastro, E. Smecca, S. Sanzaro, I. Deretzis, A. La Magna, Y. Numata, A. K. Jena, T. Miyasaka, A. Gagliano, A. Alberti, *Front. Chem.* **2020**, *200*.
- [10] A. K. Jena, Y. Numata, M. Ikegami, T. Miyasaka, *J. Mater. Chem. A* **2018**, *6*, 2219.
- [11] M. Ulfa, P. Wang, J. Zhang, J. Liu, W. D. De Marcillac, L. Coolen, S. Peralta, T. Pauporté, *ACS Appl. Mater. Interfaces* **2018**, *10*, 35118.
- [12] S. Sanzaro, E. Smecca, G. Mannino, C. Bongiorno, G. Pellegrino, F. Neri, G. Malandrino, M. R. Catalano, G. G. Condorelli, R. Iacobellis, L. De Marco, C. Spinella, A. La Magna, A. Alberti, *Sci. Rep.* **2016**, *6*, 39509.
- [13] A. Alberti, E. Smecca, S. Sanzaro, C. Bongiorno, F. Giannazzo, G. Mannino, A. La Magna, M. Liu, P. Vivo, A. Listorti, E. Calabrò, F. Matteocci, A. Di Carlo, *ACS Appl. Energy Mater.* **2019**, *2*, 6218.
- [14] E. Smecca, Y. Numata, I. Deretzis, G. Pellegrino, S. Boninelli, T. Miyasaka, A. La Magna, A. Alberti, *Phys. Chem. Chem. Phys.* **2016**, *18*, 13413.
- [15] G. Mannino, I. Deretzis, E. Smecca, A. La Magna, A. Alberti, D. Ceratti, D. Cahen, *J. Phys. Chem. Lett.* **2020**, *11*, 2490.
- [16] I. Spanopoulos, W. Ke, C. C. Stoumpos, E. C. Schueller, O. Y. Kontsevoi, R. Seshadri, M. G. Kanatzidis, *J. Am. Chem. Soc.* **2018**, *140*, 5728.
- [17] W. Xiang, W. Tress, *Adv. Mater.* **2019**, *31*, 1902851.
- [18] Z. Guo, A. K. Jena, I. Takei, G. M. Kim, M. A. Kamarudin, Y. Sanehira, A. Ishii, Y. Numata, S. Hayase, T. Miyasaka, *J. Am. Chem. Soc.* **2020**, *142*, 9725.
- [19] G. Fiscaro, A. La Magna, A. Alberti, E. Smecca, G. Mannino, I. Deretzis, *J. Phys. Chem. Lett.* **2020**, *11*, 1068.
- [20] X. Chang, J. Fang, Y. Fan, T. Luo, H. Su, Y. Zhang, J. Lu, L. Tsetseris, T. D. Anthopoulos, S. Liu, K. Zhao, *Adv. Mater.* **2020**, *32*, 2001243.
- [21] A. Marronnier, G. Roma, S. Boyer-Richard, L. Pedesseau, J. M. Jancu, Y. Bonnassieux, C. Katan, C. C. Stoumpos, M. G. Kanatzidis, *J. Even, ACS Nano* **2018**, *12*, 3477.
- [22] D. B. Straus, S. Guo, A. M. Abeykoon, R. J. Cava, *Adv. Mater.* **2020**, *32*, 2001069.
- [23] A. Dutta, N. Pradhan, *ACS Energy Lett.* **2019**, *4*, 709.
- [24] C. F. J. Lau, X. Deng, J. Zheng, J. Kim, Z. Zhang, M. Zhang, J. Bing, B. Wilkinson, L. Hu, R. Patterson, S. Huang, A. Ho-Baillie, *J. Mater. Chem. A* **2018**, *6*, 5580.
- [25] S. Xiang, W. Li, Y. Wei, J. Liu, H. Liu, L. Zhu, H. Chen, *Nanoscale* **2018**, *10*, 9996.
- [26] Y. Hu, F. Bai, X. Liu, Q. Ji, X. Miao, T. Qiu, S. Zhang, *ACS Energy Lett.* **2017**, *2*, 2219.
- [27] A. K. Jena, A. Kulkarni, Y. Sanehira, M. Ikegami, T. Miyasaka, *Chem. Mater.* **2018**, *30*, 6668.
- [28] R. K. Behera, A. Dutta, D. Ghosh, S. Bera, S. Bhattacharyya, N. Pradhan, *J. Phys. Chem. Lett.* **2019**, *10*, 7916.
- [29] R. J. Sutton, M. R. Filip, A. A. Haghighirad, N. Sakai, B. Wenger, F. Giustino, H. J. Snaith, *ACS Energy Lett.* **2018**, *3*, 1787.
- [30] D. B. Straus, S. Guo, R. J. Cava, *J. Am. Chem. Soc.* **2019**, *141*, 11435.
- [31] Q. Ye, Y. Zhao, S. Mu, F. Ma, F. Gao, Z. Chu, Z. Yin, P. Gao, X. Zhang, J. You, *Adv. Mater.* **2019**, *31*, 810.
- [32] D. G. Nocera, L. R. Morss, J. A. Fahey, *J. Inorg. Nucl. Chem.* **1980**, *42*, 55.
- [33] W. Li, B. Zhu, N. Pai, W. Mao, T. Zhang, Q. Bao, X. Wen, U. Bach, M. U. Rothmann, A. Liu, W. Chen, Y. Y. Choo, J. Etheridge, Y.-B. Cheng, *Sci. China Mater.* **2016**, <https://doi.org/10.1007/s40843-021-1660-6>.
- [34] J. A. Mundy, D. Hodash, A. Melville, R. Held, T. Mairoser, D. A. Muller, L. F. Kourkoutis, A. Schmehl, D. Schlom, *Appl. Phys. Lett.* **2014**, *104*, 091601.

- [35] Y.-H. Kye, C.-J. Yu, U.-G. Jong, K.-C. Ri, J.-S. Kim, S.-H. Choe, S.-N. Hong, S. Li, J.N. Wilson, A. Walsh, *J. Phys. Chem. C* **2019**, *123*, 9735.
- [36] C. Wang, A. S. R. Chesman, J. J. Jasieniak, *Chem. Commun.* **2017**, 53, 232.
- [37] Q. Zhao, A. Hazarika, L. T. Schelhas, J. Liu, E. A. Gaulding, G. Li, M. Zhang, M. F. Toney, P. C. Sercel, J. M. Luther, *ACS Energy Lett.* **2020**, *5*, 238.
- [38] G. Mannino, A. Alberti, I. Deretzis, E. Smecca, S. Sanzaro, Y. Numata, T. Miyasaka, A. La Magna, *J. Phys. Chem. C* **2017**, *121*, 7703.
- [39] P. Y. Yu, M. Cardona, *Fundamentals of Semiconductors Physics and Materials Properties*, 4th ed., Springer, Berlin/New York **2010**.
- [40] L. Viña, S. Logothetidis, M. Cardona, *Phys. Rev. B* **1984**, *30*, 1979.
- [41] S. Logothetidis, L. Via, M. Cardona, *Phys. Rev. B* **1985**, *31*, 947.
- [42] P. Lautenschlager, M. Garriga, M. Cardona, *Phys. Rev. B* **1987**, *36*, 4813.
- [43] P. Lautenschlager, M. Garriga, L. Vina, M. Cardona, *Phys. Rev. B* **1987**, *36*, 4821.
- [44] B. Zhao, S. F. Jin, S. Huang, N. Liu, J. Y. Ma, D. J. Xue, Q. Han, J. Ding, Q. Q. Ge, Y. Feng, J. S. Hu, *J. Am. Chem. Soc.* **2018**, *140*, 11716.
- [45] P. Giannozzi, S. Baroni, N. Bonini, M. Calandra, R. Car, C. Cavazzoni, D. Ceresoli, G. L. Chiarotti, M. Cococcioni, I. Dabo, A. Dal Corso, S. De Gironcoli, S. Fabris, G. Fratesi, R. Gebauer, U. Gerstmann, C. Gougoussis, A. Kokalj, M. Lazzeri, L. Martin-Samos, N. Marzari, F. Mauri, R. Mazzarello, S. Paolini, A. Pasquarello, L. Paulatto, C. Sbraccia, S. Scandolo, G. Sclauzero, A. P. Seitsonen, A. Smogunov, P. Umari, R. M. Wentzcovitch, *J. Phys. Condens. Matter* **2009**, *21*, 395502.
- [46] J. P. Perdew, K. Burke, M. Ernzerhof, *Phys. Rev. Lett.* **1996**, *77*, 3865.
- [47] H. J. Monkhorst, J. D. Pack, *Phys. Rev. B* **1976**, *13*, 5188.
- [48] K. Momma, F. Izumi, *J. Appl. Crystallogr.* **2011**, *44*, 1272.